High-resolution absorption spectroscopy of the OH 2Pi 3/2 ground state line

Helmut Wiesemeyer, Rolf Güsten, Stefan Heyminck, Karl Jacobs, Karl Menten, David Neufeld, Miguel Angel Requena-Torres, Jürgen Stutzki

Letter to the Editor

High-resolution absorption spectroscopy of the OH $^2\Pi_{3/2}$ ground state line

H. Wiesemeyer[1], R. Güsten[1], S. Heyminck[1], K. Jacobs[2], K.M. Menten[1], D.A. Neufeld[3], M.A. Requena-Torres[1], and J. Stutzki[2]

1. Max-Planck-Institut für Radioastronomie, Auf dem Hügel 69, 53121 Bonn, Germany
   e-mail: hwiese@mpifr.de
2. I. Physikalisches Institut, Universität zu Köln, Zülpicher Str. 77, 50937 Köln, Germany
3. The Johns Hopkins University, 3400 North Charles St. Baltimore, MD 21218, USA

Received ; accepted

ABSTRACT

The chemical composition of the interstellar medium is determined by gas phase chemistry, assisted by grain surface reactions, and by shock chemistry. The aim of this study is to measure the abundance of the hydroxyl radical (OH) in diffuse spiral arm clouds as a contribution to our understanding of the underlying network of chemical reactions. Owing to their high critical density, the ground states of light hydrides provide a tool to directly estimate column densities by means of absorption spectroscopy against bright background sources. We observed onboard the SOFIA observatory the $^2\Pi_{3/2}$, $J = 5/2 \leftarrow 3/2$ 2.5 THz line of ground-state OH in the diffuse clouds of the Carina-Sagittarius spiral arm. OH column densities in the spiral arm clouds along the sightlines to W49N, W51 and G34.26+0.15 were found to be of the order of 10^{14} cm^{-2}, which corresponds to a fractional abundance of 10^{-7} to 10^{-8}, which is comparable to that of H$_2$O. The absorption spectra of both species have similar velocity components, and the ratio of the derived H$_2$O to OH column densities ranges from 0.3 to 1.0. In W49N we also detected the corresponding line of ^{18}OH.

Key words. ISM: lines and bands, molecules, clouds

1. Introduction

The first molecule discovered in space was the CH radical (Dunham 1937). At that time, the first predictions were made regarding the abundances of molecules in interstellar space, identifying the hydroxyl radical (OH) as a promising candidate (Swings & Rosenfeld 1937). It took more than two decades until the latter was detected in the ISM (Weinreb et al. 1963), in absorption against the supernova remnant Cas A, in the $F = 1 - 1$ and $2 - 2$ transitions between the hyper-fine structure split Λ-double levels of OH's $^2\Pi_{3/2}$, $J = 3/2$ rotational ground state. Comprehensive models of the gas phase chemistry of diffuse interstellar clouds constructed by van Dishoeck & Black (1986) revealed the importance of the OH radical in the network of reactions leading to the formation of oxygen-bearing molecules. Unfortunately, OH column densities in these objects are difficult to determine from radio lines, due to frequently observed deviations of the underlying level population from LTE (e.g., Neufeld et al. 2002). The highest densities occurring in diffuse clouds amount to $\sim 10^4$ cm^{-3} (Greaves & Williams 1994), while their mean density is $\sim 10^2$ cm^{-3} (Snow & McCall 2006; Cox et al. 1988 derived upper limits of a few thousand cm^{-3}).

Storey et al. (1981) first detected the Λ doublet line from the OH ground state ($^2\Pi_{3/2}$ $J = 5/2 \leftarrow 3/2$) towards Sgr B2 near the Galactic centre with the Kuiper Airborne Observatory, but their spectral resolution (250 km s^{-1}) proved inadequate to separate the absorption by the line-of-sight clouds from that occurring in Sgr B2 itself. Here we report the detection of one doublet line of this transition (at 2514 GHz) and of its isotopolog

^{18}OH (at 2495 GHz) with GREAT[1] onboard SOFIA, in absorption towards the giant H II regions W49N and W51 and the ultracompact H II region G34.26+0.15. Both lines are inaccessible for Herschel/HIFI. The three observed lines of sight are within a 15° wide Galactic longitude interval. Those towards W51 and G34.26+0.15 cross the near side of the Carina-Sagittarius spiral arm, with W51 ($\ell = 49°.5$) at a distance of 5.41 (+0.31, −0.28) kpc (Sato et al. 2010) and G34.26+0.15 at ~ 2 kpc distance (cf. measurements of G35.10-0.74, which has a comparable radial velocity, Zhang et al. 2009). The line of sight to W49N ($\ell = 43°.2$) first crosses the near side of the Carina-Sagittarius arm, grazes the Crux-Scutum arm, and then again crosses the Carina-Sagittarius arm on its far side, where W49N is located at a distance of (11.4 ± 1.2) kpc (Gwinn et al. 1992).

2. Observations, data reduction and analysis

The observations reported here were performed with the GREAT receiver (Heyminck et al. 2012) onboard the SOFIA airborne observatory (Young et al. 2012), as part of the *basic science* programme (flights on 2011 July 26 and November 8). On the first flight the receiver's M and L2 bands were tuned to 2514.317 GHz for the $^2\Pi_{3/2}$ $J = 5/2 \leftarrow 3/2$ group of OH hyperfine structure lines (in the lower sideband) and to 1837.817 GHz for the $^2\Pi_{1/2}$ $J = 3/2 \leftarrow 1/2$ lines (in the upper sideband), respectively. On the second flight, the M band was also tuned to the 2494.695 GHz frequency of the $^2\Pi_{3/2}$ $J = 5/2 \leftarrow 3/2$ transition

---

[1] GREAT is a development by the MPI für Radioastronomie and the KOSMA/Universität zu Köln, in cooperation with the MPI für Sonnensystemforschung and the DLR Institut für Planetenforschung.

Table 1. List of the observed $^2\Pi_{3/2}$ $J = 5/2 \leftarrow 3/2$ ^{16}OH and ^{18}OH lines

Transition	Frequency [GHz][a]	A_E [s^{-1}][b]
OH, $^2\Pi_{3/2}$, $J = 5/2 \leftarrow 3/2$		
$F = 2^- \leftarrow 2^+$	2514.298092	0.0137
$F = 3^- \leftarrow 2^+$	2514.316386	0.1368
$F = 2^- \leftarrow 1^+$	2514.353165	0.1231
^{18}OH, $^2\Pi_{3/2}$, $J = 5/2 \leftarrow 3/2$		
$F = 2^+ \leftarrow 2^-$	2494.68092	0.0136
$F = 3^+ \leftarrow 2^-$	2494.69507	0.1356
$F = 2^+ \leftarrow 1^-$	2494.73421	0.1221

[a] Varberg & Evenson (1993, $\sigma_{rms} = 30$ kHz). The frequencies for ^{18}OH were derived by isotope scaling. [b] Pickett et al. (1998).
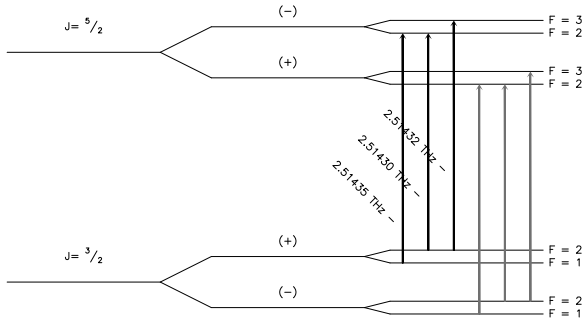
Fig. 1. Level diagram (not to scale) for the $^2\Pi_{3/2}$ OH ground and first excited state. The observed ^{16}OH transitions are indicated by bold arrows and labelled with their corresponding frequency. The observed ^{18}OH transitions are drawn as grey arrows.

of ^{18}OH. Typical DSB receiver temperatures were 4500 K and 2500 K for the M and L2 bands, respectively. Total power subtraction was performed by chopping with an amplitude of 90″ at 1 Hz. The raw data were converted from XFFT spectrometer (Klein et al. 2012) count rates to forward-beam brightness temperatures with the module *kalibrate* (Guan et al. 2012) as part of the *kosma_software* observing software, analysing the data from the calibration loads and the atmospheric total power and allowing us to fit both the wet component (typically pwv=10-20 μm) and dry content of the atmospheric emission and thus to determine the opacity correction (a few ×0.1). Further processing of the data (conversion to main-beam brightness temperature, with a beam efficiency of 0.58, and averaging with $1/\sigma_{rms}^2$ weighting) was made with the cLASS software. The overall calibration uncertainty does not exceed 20%.

Thanks to the high critical density of the $J = 5/2 \rightarrow 3/2$ transition (5.1×10^9 cm^{-3} for a 15 K gas, collision coefficients from Dewangan et al. 1987, Einstein coefficients as given in Tab. 1), we can safely expect almost all OH to be in its ground state at the density of the foreground diffuse clouds along the sight-line. This makes the determination of column densities much more reliable than those derived from the λ 18 cm line. Likewise, the $^2\Pi_{1/2}$ $J = 1/2$ level (64 K above the $^2\Pi_{3/2}$ $J = 5/2$ level) cannot be substantially populated either, because we failed to detect absorption in the simultaneously observed $^2\Pi_{1/2}$ $J = 3/2 \leftarrow 1/2$ transition. The spectral profile, in absence of emission, is thus is given by

$$T_{mb}(\upsilon) = T_{mb,c} \exp\left(-\sum_{i=1}^{N_{vc}} \sum_{j=1}^{N_{hfc}} \tau_{ij,\upsilon}\right), \quad (1)$$

Table 2. Results of the OH line profile fitting.

Source ($T_{mb,c}$)	$\upsilon_0^{[a]}$	FWHM[b]	$\tau_{max}^{[c]}$	$N_{OH}^{[d]}$
	[km s^{-1}]			[10^{14} cm^{-2}]
W49N	2.9 ± 1.9	13.4 ± 0.4	0.9	8.8 ± 4.6
(12.3 K)	12.3 ± 1.0	10.1 ± 1.1	10.1	
	36.8 ± 3.5	11.8 ± 4.4	1.8	1.6 ± 0.9
	39.1 ± 1.3	2.8 ± 0.5	2.3	0.5 ± 0.1
	60.5 ± 0.3	10.4 ± 3.9	2.5	2.0 ± 0.2
W51	7.2 ± 0.4	4.6 ± 2.2	2.9	0.66 ± 0.08
(8 K)	59.4 ± 3.3	16.8 ± 4.5	5.2	5.6 ± 2.1
	68.2 ± 1.4	4.6 ± 2.7	1.9	
G34.26+0.15	12.6 ± 0.2	5.7 ± 0.8	2.5	1.12 ± 0.21
(9 K)	28.3 ± 0.5	6.0 ± 1.6	1.4	0.67 ± 0.09
	55.4 ± 0.4	12.9 ± 1.0	4.8	4.73 ± 1.20

[a] LSR velocity of component. The first and third hyperfine component (hfc) are +2.2 and −4.4 km s^{-1}, respectively, off the second one.
[b] FWHM of Gaussian absorption profile, deconvolved from hfc split.
[c] Peak opacity in the strongest hfc. The saturated absorption towards W49N ($\upsilon_{lsr} < 25$ km s^{-1}) provides only a lower opacity limit.
[d] Column density per fitted velocity component.

where T_{mb} and $T_{mb,c}$ are the main beam brightness Rayleigh-Jeans temperatures of the spectral profile (here as a function of velocity) and of the continuum (in single-sideband calibration), respectively, and N_{vc} and N_{hfc} are the number of velocity components and hyperfine components, respectively. While uncertainties in the calibration temperature cancel out in the opacity determination, any residual offset of variance $\sigma_{rms,Tc}^2$ in the definition of the continuum level leads to an additional uncertainty in the derived opacity of $\sigma_{rms,\tau} = \sigma_{rms,T_c}/T_c$. The absorption spectra suggest $\sigma_{rms,\tau} \sim 0.1$, which is tolerable in view of the substantial opacities. A simultaneous least-squares fit to the line profiles of all velocity components (Eq. 1) with the opacity

$$\tau_{ij,\upsilon} = \sqrt{\frac{\ln 2}{\pi}} \frac{A_{E,j}c^3}{4\pi\Delta\upsilon_i\nu_j^3} \frac{g_{u,j}}{g_{l,j}} N_{OH} w_\Lambda \exp\left(-4\ln 2 \left(\frac{\upsilon - \upsilon_{0,ij}}{\Delta\upsilon_i}\right)^2\right) \quad (2)$$

yields N_{OH}, the OH column density per velocity component. Here $\Delta\upsilon_i$ is the FWHM of the Gaussian component i, $g_{u,j}$ and $g_{l,j}$ are the statistical weights ($2F + 1$) of the upper and lower level, respectively, of a given hyperfine component j, $\upsilon_{0,ij}$ is the offset of its velocity from the line-of-sight velocity of the source, and $w_\Lambda = 0.5$ corrects for the fact that only one doublet line was observed (Fig. 1). Owing to the relatively large number of free parameters ($3N_{vc}$), a simulated annealing method (Metropolis algorithm) was used in combination with a downhill simplex method (Press et al. 1992). The former assists the minimisation process in escaping from a local minimum, and the latter improves the efficiency of the convergence. The velocity structure in the para-H$_2$O $1_{11} - 0_{00}$ spectrum towards W49N (Sonnentrucker et al. 2010) suggests five velocity components as a strict minimum, while with more components, the procedure would start to fit noise features. The results are summarised in Tab. 2. The OH column density can be expressed by the relationship N_{OH} [cm^{-2}] $= 7.8 \times 10^{12} \tau_{max} \Delta\upsilon_{fwhm}$ [km s^{-1}] as a function of the opacity in the strongest hyperfine component and of the width of the absorption profile of the deconvolved spectrum. The uniqueness of the solution was tested with a Monte Carlo study, yielding the standard deviation of each parameter.

Table 3. OH and H_2O abundances and their ratios in line-of-sight clouds towards W49N and W51. Statistical errors are given in brackets.

		W49N v_{lsr} intervals [km s^{-1}]					W51 v_{lsr} intervals [km s^{-1}]		
		(30,37)	(37,44)	(44,49)	(49,54)	(54,72)	(−1,11)	(11,16)[c]	(43,50)
N_{OH}	[10^{13} cm^{-2}]	7.1(0.5)	11.3(6.3)	1.2(0.2)	1.5(0.3)	18.1(1.3)	6.4(0.9)	−	3.1(0.6)
$N_{H_2O}^{(a)}$	[10^{13} cm^{-2}]	2.3(0.1)	6.2(0.6)	0.1(0.05)	1.5(0.07)	11.6(0.4)	2.6(0.1)	0.23(0.05)	2.5(0.1)
$N_{H_2}^{(b)}$	[10^{20} cm^{-2}]	5.9(1.9)	6.6(2.0)	0.9(0.03)	3.2(0.1)	22.6(3.7)	4.3(0.1)	0.6(0.03)	2.6(0.8)
[OH]/[H$_2$]	[10^{-8}]	12.0(4.0)	17(11)	13.2(2.5)	4.5(0.9)	8.0(1.4)	15(2.1)	−	11.9(4.3)
[H$_2$O]/[H$_2$]	[10^{-8}]	3.9(1.3)	9.4(3.0)	1.1(0.6)	4.7(0.3)	5.1(0.9)	6.0(0.3)	3.8(0.9)	9.6(3.0)
[H$_2$O]/[OH]		0.32(0.03)	0.55(0.31)	0.08(0.04)	1.03(0.20)	0.64(0.05)	0.40(0.06)	−	0.81(0.16)

(a) Sonnentrucker (2010), (b) Godard et al. (2012). (c) The sensitivity of the OH observations is not sufficient for this velocity interval.

3. Results

For the spiral arm clouds there is no ambiguity in the fit results (Fig. 2). Towards the three continuum sources the absorption is saturated, i.e., in the (5, 20), (40, 80) and (35, 70) km s^{-1} velocity intervals for W49N, W51 and G34.26+015, respectively, where the derived main line opacities and column densities are to be considered lower limits. For W49N, this caveat is corroborated by the ^{18}OH absorption profile (Fig. 3). The ^{18}OH/^{16}OH abundance ratio is not expected to be affected by chemical fractionation (Langer et al. 1984). The synthesised opacity in the W49N spectrum peaks at τ= 5.7. Assuming for the ^{18}O/^{16}O ratio the value in the 4 kpc ring (327 ± 32, Wilson & Rood 1994; Polehampton et al. 2005 found no evidence of an abundance gradient with galactocentric distance), the estimated opacity in our ^{18}OH detection (τ~0.2) would require the main line opacity to be higher by at least an order of magnitude with respect to that estimated by the absorption profile fit. Unfortunately, in the 30-40 km s^{-1} velocity range the ^{18}OH absorption is affected by a telluric ozone feature, and a confirmation by observations of sources with a more favourable velocity is planned to definitely rule out a baseline ripple. In the unsaturated wings of the absorption profile, the sensitivity of the corresponding ^{18}OH measurement is no longer sufficient to estimate the ^{18}OH/OH abundance ratio. A two-component fit to the ^{18}OH absorption (Fig. 3) yields a column density of 4×10^{13} cm^{-2} for the whole absorption feature. Although the spiral arm clouds along the sight-line exhibit substantial opacities on the order of unity, the absorption is not saturated and OH column densities can be derived whose accuracy only depends on the signal-to-noise ratio, the quality of the fitted profile, and the assumed continuum level. For a comparison of our OH column densities with those observed for H_2O (Sonnentrucker et al. 2010) and inferred for H_2 (Godard et al. 2012), the absorption profiles of the clouds towards W49N and W51 are integrated within the velocity intervals of Tab. 3. With the exception of a velocity interval with an abnormally low water abundance, probably due to a spectral baseline problem, the H_2O/OH ratios are in the range 0.3-1.0. Plume et al. (2004) have determined the H_2O/OH ratio by a comparison of submillimeter H_2O observations with ground-based radio observations of the 18 cm transitions within the ground rotational state of OH. They thereby estimated a H_2O/OH ratio of 0.4 at v_{lsr}=68 km s^{-1}, in agreement with our measurement of 0.6. The ratio of ~0.3 measured by Neufeld et al. (2002) towards W51, at v_{lsr}=6 km s^{-1}, compares to our value of 0.4 in the v_{lsr}=(−1,11) km s^{-1} interval. Their OH column density is compatible with our value (8×10^{13} cm^{-2} and 6.4×10^{13} cm^{-2}, respectively). Observations of the $^2\Pi_{1/2} \leftarrow ^2\Pi_{3/2}$ cross-band transitions towards Sgr B2 (Polehampton et al. 2005) suggest a H_2O/OH range of 0.6-1.2.

Generally, discrepancies between different sets of data may be due to NLTE effects in the radio lines, different spectral resolutions and definitions of velocity components, and uncertainties in the definition of the respective continuum levels.
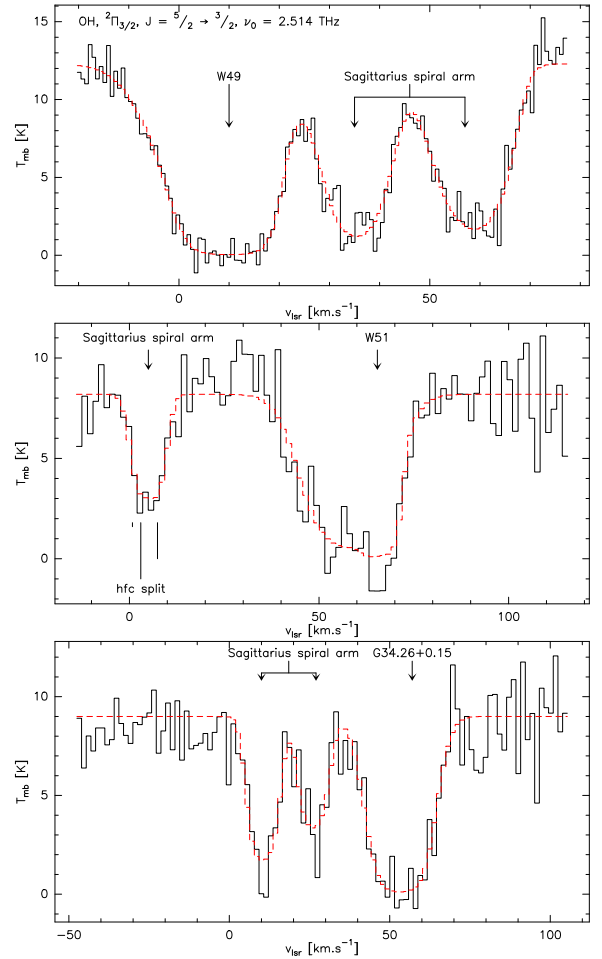
Fig. 2. Top: OH absorption towards W49N. The velocities of the line-of-sight clouds and of W49N are indicated. The red dashed line is a least-squares fit. **Middle:** Same for the OH absorption against W51e4. The relative positions and strengths of the hfc splitting are indicated for the v_{lsr}=7 km s^{-1} component. **Bottom:** OH absorption against G34.26+0.15.
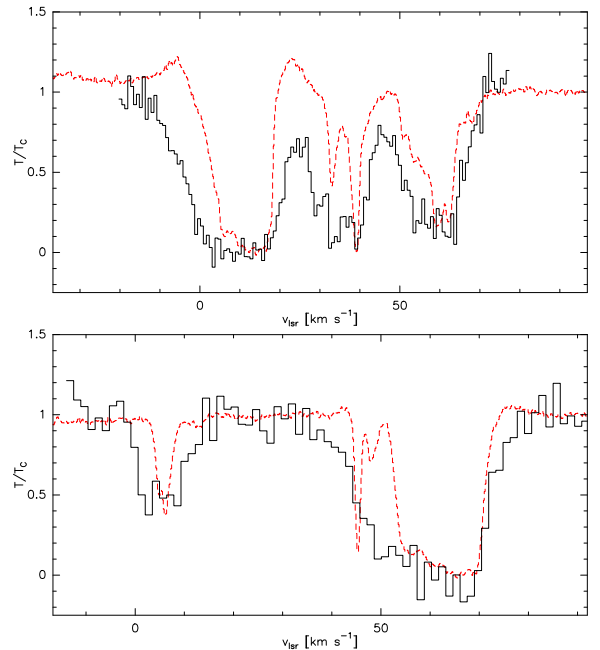
The chemistry leading to interstellar OH and water has been considered in many theoretical studies over the past thirty years (e.g. Draine et al. 1983; van Dishoeck & Black
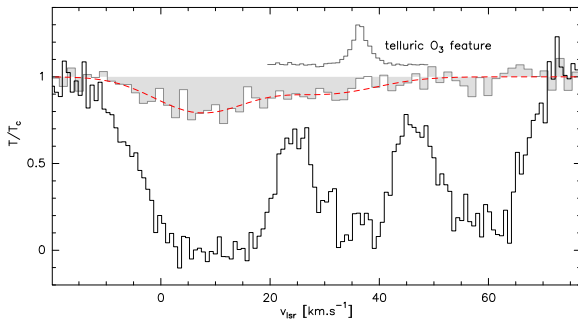
Fig. 3. ^{18}OH absorption (top, grey-shaded), a least-squares, two-component fit to it (dashed line) and OH absorption towards W49N. The spectra are scaled by the corresponding continuum level, to facilitate a comparison. The insert at the top shows a telluric ozone feature (as observed in total power), where the calibration is more uncertain.

Fig. 4. Para-H_2O absorption (dashed red line; from Sonnentrucker et al. 2010) and OH absorption (solid line), normalised by the respective single sideband continua, towards W49N (top) and W51 (bottom).

1986; Hollenbach et al. 2009, and references therein). Three main pathways to OH have been identified in diffuse and translucent molecular clouds. The first pathway involves an ion-molecule chemistry, initiated by the cosmic-ray ionization of H_2 or H. The resulting H_2^+ and H^+ ions can lead to OH^+ through the reaction sequences $H_2^+(H_2, H)H_3^+(O, H_2)OH^+$ or $H^+(O, H)O^+(H_2, H)OH^+$. In clouds with a low molecular fraction, the resulting OH^+ is destroyed primarily by dissociation recombination with electrons. In clouds with a high molecular fraction, however, OH^+ is rapidly converted to H_3O^+ by a series of two H atom abstraction reactions: $OH^+(H_2, H)H_2O^+(H_2, H)H_3O^+$. The H_3O^+ ion then undergoes dissociative recombination with electrons to form OH or H_2O. The branching ratio for this process is important in determining the resultant OH/H_2O ratio and has been studied in two recent ion storage ring experiments (Jensen et al. 2000; Neau et al. 2000): these suggest that ~74% to 83% of dissociative recombinations lead to OH, with almost all the remainder leading to H_2O (and less than ~1% resulting in the production of O). In diffuse or translucent clouds, both neutral molecules are destroyed by photodissociation, which - in the case of H_2O - is an additional formation process for OH. A second and different pathway may be important in shocks or turbulent dissipation regions, where elevated gas temperatures can drive a series of neutral-neutral reactions with significant energy barriers: $O(H_2, H)OH(H_2, H)H_2O$. Finally, OH and H_2O may be produced by means of a grain-surface chemistry, in which O nuclei are hydrogenated on grain surfaces and subsequently photodesorbed. The relative importance of these three pathways will determine the exact H_2O/OH abundance ratio, but all three predict a close relationship between OH and H_2O. This relationship is supported by the observations reported here, which indicate a good correspondence between the OH and H_2O absorption features; detailed modelling, which must await a larger sample of sight-lines, will be needed to interpret observed variations in the H_2O/OH ratio. We note, however, that the lower end of the observed range of H_2O/OH ratios (0.3-1.0) is predicted by models for turbulent chemistry (Godard et al. 2009). We note also that the observed distribution of OH is quite different from that of OH^+; the latter is believed to arise primarily in material with a molecular fraction that is too low to permit the efficient production of H_3O^+, whereas the former will arise in clouds with a substantial abundance of H_2.

Future data of the OH ground state transition and the relatively high precision of the resulting column densities will not only allow us to assess the correlation between the abundances of OH and H_2O, but also to re-calibrate less accurate OH column densities derived from decades of radio observations.

References

Cox, P., Guesten, R., & Henkel, C. 1988, A&A, 206, 108
Dewangan, D.P., Flower, D.R. & Alexander, M.H. 1987, MNRAS, 226, 505
Draine, B. T., Roberge, W. G., & Dalgarno, A. 1983, ApJ, 264, 485
Dunham, T., Jr. 1937, PASP, 49, 26
Godard, B., Falgarone, E., Gerin, M., et al. 2012, A&A, 540, A87
Godard, B., Falgarone, E., & Pineau Des Forêts, G. 2009, A&A, 495, 847
Greaves, J. S., & Williams, P. G. 1994, A&A, 290, 259
Guan, X., Stutzki, H., Graf, U., et al. 2012, A&A, 542, L4
Gwinn, C. R., Moran, J. M., & Reid, M. J. 1992, ApJ, 393, 149
Heyminck, S., Graf, U.U, Güsten, R., Stutzki, J., et al. 2012, A&A, 542, L1
Hollenbach, D., Kaufman, M. J., Bergin, E. A., et al. 2009, ApJ, 690, 1497
Jensen, M. J., Bilodeau, R. C., Safvan, C. P., et al. 2000, ApJ, 543, 764
Klein, B., Hochgürtel, S., Krämer, I., et al. 2012, A&A, 542, L3
Langer, W. D., Graedel, T. E., Frerking, M. A., et al. 1984, ApJ, 277, 581
Neau, A., Al Khalili, A., Rosén, S., et al. 2000, J. Chem. Phys., 113, 1762
Neufeld, D. A., Goicoechea, J. R., Sonnentrucker, P., et al. 2010, A&A, 521, L10
Neufeld, D. A., Kaufman, M. J., Goldsmith, P. F., et al. 2002, ApJ, 580, 278
Pickett, H. M., Poynter, R. L., Cohen, E. A., et al. 1998, JQSRT, 60, 883
Plume, R., Kaufman, M. J., Neufeld, D. A., et al. 2004, ApJ, 605, 247
Polehampton, E. T., Baluteau, J.-P., & Swinyard, B. M. 2005, A&A, 437, 957
Press, W. H., et al. 1992, *Numerical Recipes (2nd ed.)*, Cambridge: Univ. Press
Sato, M., Reid, M. J., Brunthaler, A., & Menten, K. M. 2010, ApJ, 720, 1055
Snow, T. P., & McCall, B. J. 2006, ARA&A, 44, 367
Sonnentrucker, P., Neufeld, D. A., Phillips, T. G., et al. 2010, A&A, 521, L12
Storey, J. W. V., Watson, D. M., & Townes, C. H. 1981, ApJ, 244, L27
Swings, P., & Rosenfeld, L. 1937, ApJ, 86, 483
van Dishoeck, E. F., & Black, J. H. 1986, ApJS, 62, 109
Varberg, T.D.,& Evenson, K.M. 1993, Journ.Mol.Spec. 157, 55
Weinreb, S., Barrett, A. H., Meeks, M. L., & Henry, J. C. 1963, Nature, 200, 829
Wilson, T. L., & Rood, R. 1994, ARA&A, 32, 191
Young, E. T., Becklin, E. E., Marcum, P. M., et al. 2012, ApJ, 749, L17
Zhang, B., Zheng, X. W., Reid, M. J., et al. 2009, ApJ, 693, 419